The feasibility of using microwave-induced thermoacoustic tomography for detection and evaluation of renal calculi

2010 Phys. Med. Biol. 55 5203

(http://iopscience.iop.org/0031-9155/55/17/020)

IOP PUBLISHING PHYSICS IN MEDICINE AND BIOLOGY

Phys. Med. Biol. **55** (2010) 5203–5212 doi:10.1088/0031-9155/55/17/020

The feasibility of using microwave-induced thermoacoustic tomography for detection and evaluation of renal calculi

Caijun Cao, Liming Nie, Cunguang Lou and Da Xing

MOE Key Laboratory of Laser Life Science and Institute of Laser Life Science, College of Biophotonics, South China Normal University, Guangzhou 510631, People's Republic of China

E-mail: xingda@scnu.edu.cn

Received 22 April 2010, in final form 4 July 2010
Published 16 August 2010
Online at stacks.iop.org/PMB/55/5203

Abstract

Imaging of renal calculi is important for patients who suffered a urinary calculus prior to treatment. The available imaging techniques include plain x-ray, ultrasound scan, intravenous urogram, computed tomography, etc. However, the visualization of a uric acid calculus (radiolucent calculi) is difficult and often impossible by the above imaging methods. In this paper, a new detection method based on microwave-induced thermoacoustic tomography was developed to detect the renal calculi. Thermoacoustic images of calcium oxalate and uric acid calculus were compared with their x-ray images. The microwave absorption differences among the calcium oxalate calculus, uric acid calculus and normal kidney tissue could be evaluated by the amplitude of the thermoacoustic signals. The calculi hidden in the swine kidney were clearly imaged with excellent contrast and resolution in the three orthogonal thermoacoustic images. The results indicate that thermoacoustic imaging may be developed as a complementary method for detecting renal calculi, and its low cost and effective feature shows high potential for clinical applications.

(Some figures in this article are in colour only in the electronic version)

1. Introduction

In recent years, renal calculi has become widespread and serious. Renal calculi, regarded as one of the most painful urologic confusions, can lead to renal dysfunction that often causes dysuria and urinary frequency (Coe *et al* 2005). In order to reduce patients' endless suffering from the disease, it is important to localize and detect the occult object accurately and promptly. Hence, imaging investigations play an important role in the detection of renal calculi. Among renal calculi, calcium oxalate calculus is the most common type, for which

x-ray or extracorporeal shock wave lithotripsy (ESWL) can be applied for observation and treatment (Rao 2004). However, uric acid calculus is invisible to x-ray films, due to its soft-tissue-like density. Moreover, x-ray and computed tomography (CT) are insecure due to their ionizing radiation character, especially for patients who need long-term monitoring of renal calculi diseases. Ultrasound is usually applied to detect the radiolucent calculi; however, it has poor contrast in tissue and is particularly inefficient in detecting small calculi (Rao 2004, Jin *et al* 2008). In order to overcome these shortcomings, a novel method with relatively high precision should be explored and researched as a replacement.

Here we introduce a method for detecting renal calculi using microwave-induced thermoacoustic tomography (MI-TAT). The application of MI-TAT in biological tissues has been studied for many years (Kruger *et al* 1999, Ciocan and Jiang 2004, Ku *et al* 2005). However, this is the first time the detection of renal calculi using MI-TAT is being presented. A thermoacoustic signal is generated by the microwave-induced thermal expansion effect. When a biological tissue is irradiated with microwave pulses, a small time-dependent temperature variation can be observed. Thermoacoustic pressure waves are then generated due to the thermal expansion of the medium. By detecting and processing the acoustic wave, the absorber structure can be reconstructed based on the differences in the microwave absorption of the target (Ku and Wang 2000). MI-TAT may provide wider medical applications owing to its radiation imaging mechanism like water and ion distribution and deep tissue penetration. For a pulse laser, the penetration depth in biological tissue is several millimeters, while microwave radiation penetrates much more deeply into the biological tissue (Nie *et al* 2008, 2009). For a microwave at the frequency of 1.2 GHz, the penetration depths for the fat and muscle are 14 cm and 2.4 cm, respectively. For a 6 GHz microwave, the penetration depth would be a little lower than the numeric values of the 1.2 GHz microwave (Johnson and Guy 1972). Therefore, MI-TAT has a potential to be applied in renal calculi imaging deeply seated in the body (Feng *et al* 2001).

In this paper, a thermoacoustic tomography system with a 128-element linear transducer array was used to detect the uric acid calculus *in vitro*. The renal calculi hidden in the swine kidney were clearly reconstructed with high contrast and resolution in three orthogonal thermoacoustic images. Good contrast was obtained between the renal calculi and the kidney tissue, and the thermoacoustic images of the location and size of the tested targets were in good agreement with the actual sample. The results indicate that thermoacoustic imaging has the potential to be developed as a complementary method for detecting renal calculi.

2. Theory

The thermoacoustic effect refers to the generation of acoustic waves by pulsed electromagnetic (EM) irradiation, such as optical or microwave/radio frequency waves. A transient temperature rise on the order of 10 mK could be observed due to the energy deposition through the absorption of incident EM pulses. The sound or stress wave is produced as a consequence of the expansion induced by the temperature variation (Yuan and Jiang 2006). When a small renal calculus was embedded in normal kidney tissue, the thermoacoustic pressure P_a is proportional to the local absorbed microwave energy

$$P_a \propto I_o \frac{2\mu_\alpha \exp(-2\mu_\alpha d)}{\sqrt{d}}, \tag{1}$$

where μ_α is the electric field absorption coefficient of tissue, I_o is the microwave energy density at the output port of the tapered waveguide and d is the vertical distance from the output port of the microwave to the sample. The normal tissue and renal calculi have

different absorption coefficients, and the excited thermoacoustic signals can be expressed by the following expression:

$$U \propto I_o \frac{2(\mu_{\alpha p} - \mu_{\alpha q}) \exp(-2\mu_{\alpha q} d)}{\sqrt{d}}, \tag{2}$$

where $\mu_{\alpha p}$ and $\mu_{\alpha q}$ represent the microwave-absorption coefficients of the renal calculi and the normal kidney tissue, respectively (Ku and Wang 2001).

The microwave energy absorbed by biological tissue is determined by the dielectric properties, conductivity s and permittivity ε relative to free space (Gabriel *et al* 1996, Guo *et al* 2007, Pelster 2008, Xu *et al* 2003). Different absorption within the tissue produces different energy deposition, followed by rapid thermal expansion. This thermal expansion produces acoustic pressure waves, which propagate through the tissue in all directions roughly at a velocity of 1.5×10^5 cm s^{-1} (Jin and Wang 2006, Zhang and Wang 2008). The uric acid calculus has stronger microwave absorption than the kidney tissue, and the calcium oxalate calculus has much weaker absorption than the kidney tissue. The microwave absorption differences of the calcium oxalate, uric acid calculus and normal kidney tissue can be evaluated by the amplitude of thermoacoustic signals, which can be approximately written as (Park *et al* 1996, Sigrist 1986)

$$P = \Gamma \mu_a I_o, \tag{3}$$

where Γ is the Grüneisen constant ($\Gamma = \left(\beta c_o^2 / C_p\right)$, β is the isobaric volume expansion coefficient, c_o is the speed of ultrasound and C_p is the specific heat). The expression indicates that the amplitude of the thermoacoustic signal is proportion to the microwave-absorption coefficient. With the amplitude of thermoacoustic signals differences, we can detect the renal calculi buried in the kidney tissue. In the experiment, the 1.2 GHz microwave generator was employed as the excitation source due to its much better penetration ability.

3. Materials and methods

3.1. Experimental setup

A schematic of the experimental setup for MI-TAT is illustrated in figure 1(a). The microwave source has a frequency of 1.2 GHz (BW-1200HPT, China), with a pulse duration of 0.5 μs, and the peak power was estimated to be 300 kW. The pulse energy used in the experiments was estimated to be around 150 mJ (=300 kW $\times$ 0.5 μs) (Lou and Xing 2010), within the IEEE safety standards (IEEE Standard 2005). The microwave pulses were coupled into a rectangular waveguide with a cross-section of 12.7×6.3 cm^2 and achieve uniform irradiation on the sample surface. The energy density was adjusted to 1.88 mJ cm^{-2}. The energy dosage was less than the 'maximum permissible exposure' (MPE) of 30 mJ cm^{-2} for human skin at this wavelength according to the American National Standards Institute (ANSI) standard.

The data-acquisition system was mainly composed of B-mode digital ultrasound diagnostic equipment (Model CTS-5000B, SIUI, China). A 128-element transducer (L2L50A) and a high-speed digital data-acquisition system card (DASC) (PCI-6541, NI, USA) were used for data collection. The digital B-mode ultrasound diagnostic equipment with a 128-element transducer array was used for detecting the original thermoacoustic signals (Yang *et al* 2007a, 2007b, Yin *et al* 2004, Lao *et al* 2008). The linear transducer array has a central frequency of 2.5 MHz with a nominal bandwidth of 70% (Nie *et al* 2007, 2008). The signals from the transducer were acquired with the DASC and then transferred to a personal computer for subsequent data processing.

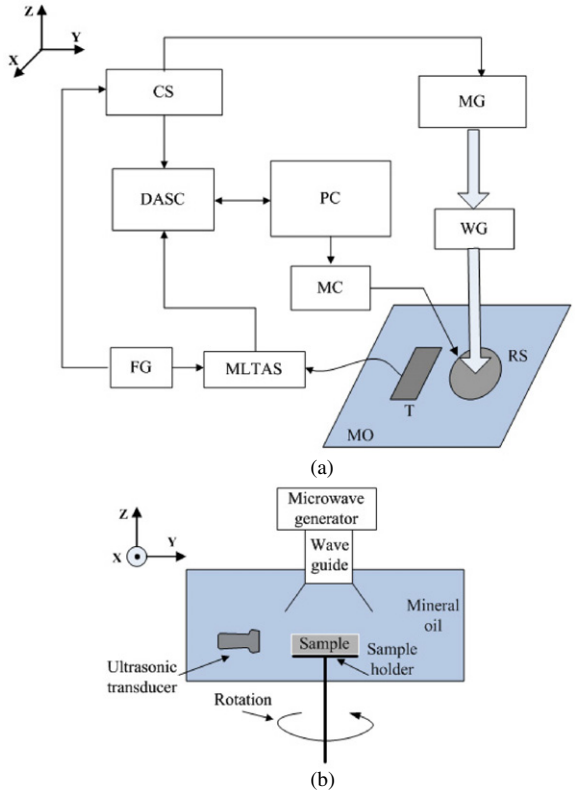

Figure 1. Experimental setup of thermoacoustic tomography. (a) Schematic of the experimental setup. MG, microwave generator; WG, waveguide; CS, clock signal; DASC, data acquisition system card; FG, function generator; MC, motor controller; MLTAS, multi-element linear transducer array system; MO, mineral oil; RS, rotation stage; PC, computer; T, ultrasonic transducer. (b) Side view of the experimental setup.

The function generator provided a synchronized clock to trigger the microwave generator and the DASC. With the multi-way electronic switch of a multi-element linear transducer array system (MLTAS), the control circuit selected several elements of the linear transducer array to capture the thermoacoustic signal. The multi-way signals were then delivered to the computer for subsequent processing. The motor drove the rotation stage with the sample for circular scanning. The whole process including data collection and motor driving was controlled by the computer based on the platform of LABVIEW (Guo and Yang 2009). The thermoacoustic image can be reconstructed by many algorithms (Haltmeier *et al* 2004, 2005, Finch and Rakesh 2007, Xu and Wang 2002, Stefanov and Uhlmann 2009), and the reconstructed two-dimensional thermoacoustic image used in this paper was based on the improved limited-field-filtered back-projection (LFBP) algorithm (Yang *et al* 2005, Wang *et al* 2004).

A side view of the experimental setup is shown in figure 1(b). A Cartesian coordinate system is set up for reference: the x axis points outward perpendicularly to the drawing plane; the y axis points to the right and the z axis points upward along the rotation axis. A polyvinyl chloride tank was employed and transformer oil was used to couple the thermoacoustic waves to the transducer. The to-be-imaged sample was placed on a rotary stage and controlled by

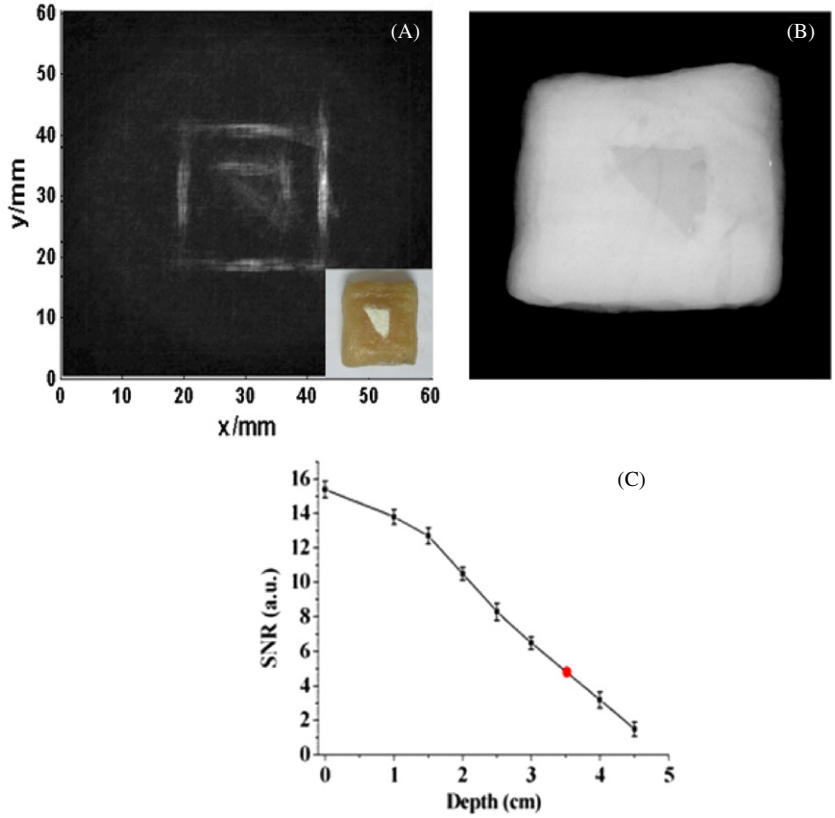

Figure 2. The thermoacoustic and x-ray imaging of a simulated sample made of uric acid powder embedded in chicken breast tissue. (A) Thermoacoustic image of the sample. (B) X-ray image of the sample. (C) Calculated SNR for imaging the uric acid 'calculus' embedded in biological tissue at different depths. The (red) dot implies the better depth for thermoacoustic imaging with enough SNR for image reconstruction.

a stepping motor with a step size of 18°. The total data at 20 circular scanning stops were acquired to reconstruct a clear and accurate image.

3.2. Pathological model

The materials used in the experiments were calcium oxalate and uric acid calculus. The calcium oxalate calculus was removed from the patients in the hospital of Jinan University. The uric acid calculus, which was ablated during the operation in hospital, was simulated with the mixture of uric acid powder and a very small amount of lard. In figure 2, the simulated uric acid calculus was made in the shape of a triangle. A piece of homogeneous chicken breast tissue was made into an arbitrary shape. Then, a screwdriver was used to carefully carve a pouch. The uric acid sample was placed in the modified chicken breast tissue and the sample was covered by another piece of chicken breast tissue with 3 cm thickness. The swine kidney was employed in the next experiment. A small screwdriver was used to carefully make holes on the swine kidney to place the model of renal calculi for thermoacoustic imaging.

3.3. Comparison with x-ray imaging

To validate the applicability of x-ray detection of renal calculi, x-ray imaging was taken by a digital, animal-used x-ray system (piXarray 100 digital specimen radiography systems, Bioptics, Inc., Tucson, AZ). Thermoacoustic tomography of uric acid and calcium oxalate calculus in the swine kidney was carried out using MI-TAT and compared with the corresponding x-ray imaging.

4. Results and discussion

The thermoacoustic imaging, x-ray imaging and the photograph of a phantom made of uric acid powder in the chicken breast tissue are shown in figure 2. The reconstructed thermoacoustic image of the phantom with a triangular uric acid sample within the chicken breast tissue is visualized in figure 2(A), with the cross-section of the sample shown in the inset. The geometrical shape of the triangular uric acid sample is in good agreement with the real subject and its boundary is clearly resolved. Figure 2(B) shows the x-ray image of the uric acid sample. The morphology of the chicken breast tissue is well illustrated whereas the uric acid sample to be detected is unrecognizable. The results in figure 2 demonstrate that the MI-TAT is capable of imaging the uric acid calculus with good contrast compared with x-ray imaging.

Figure 2(C) shows the signal-to-noise ratio (SNR) of the uric acid calculus embedded in the chicken breast tissue at different depths. The SNR depicts how much a signal has been corrupted by noise, is defined as SNR $= A_s/A_n$, where A_s is the average amplitude of the microwave signal and A_n is the average amplitude of undesired noise. The (red) dot indicates a depth at which the SNR of 5 can be achieved. This value should be sufficient for high-contrast imaging. The microwave intensity attenuation will increase with increasing location depth of the renal calculus, which results in the decrease of the SNR. The signal induced by the attenuated microwave energy may be compensated by the increasing microwave absorption contrast between the renal calculus and the normal kidney tissues.

To validate the ability of thermoacoustic imaging to detect the renal calculi, two different kinds of renal calculi were chosen: calcium oxalate calculus and simulated uric acid calculus. The two kinds of renal calculi put inside the swine kidney were imaged by MI-TAT and x-ray imaging. Since the waveguide area was limited for illuminating the whole kidney, a part of swine kidney was cut by a medical scalpel for experiments. Then, the renal calculi were embedded in the swine kidney using a screwdriver.

We conducted three sets of control experiments. Figure 3(A) and (A1) show the thermoacoustic image and x-ray image of the swine kidney. Since the 128-element transducer array has a computed tomography ability along the vertical direction, thermoacoustic image slices of the sample can be acquired. As can be seen from these images, the thermoacoustic image can clearly show the boundary of the swine kidney without renal calculi, and the x-ray image is also obvious. The outer bright rings in the thermoacoustic image represent the boundary between the normal kidney tissue and the surrounding mineral oil. It is equivalent to the beginning of the absorption stepper border, which brings the promotion effect (Nie *et al* 2009).

The uric acid calculus is placed inside the swine kidney for thermoacoustic imaging and x-ray imaging shown in figure 3(B) and (B1). The x-ray image of the uric acid calculus is rather blurred and even invisible, while its contour is clearly shown in the thermoacoustic image. The absorption coefficients of the uric acid calculus and kidney tissue for MI-TAT at 1.2 GHz span a great range, whereas those for x-ray imaging span a range of less than 1.5:1.

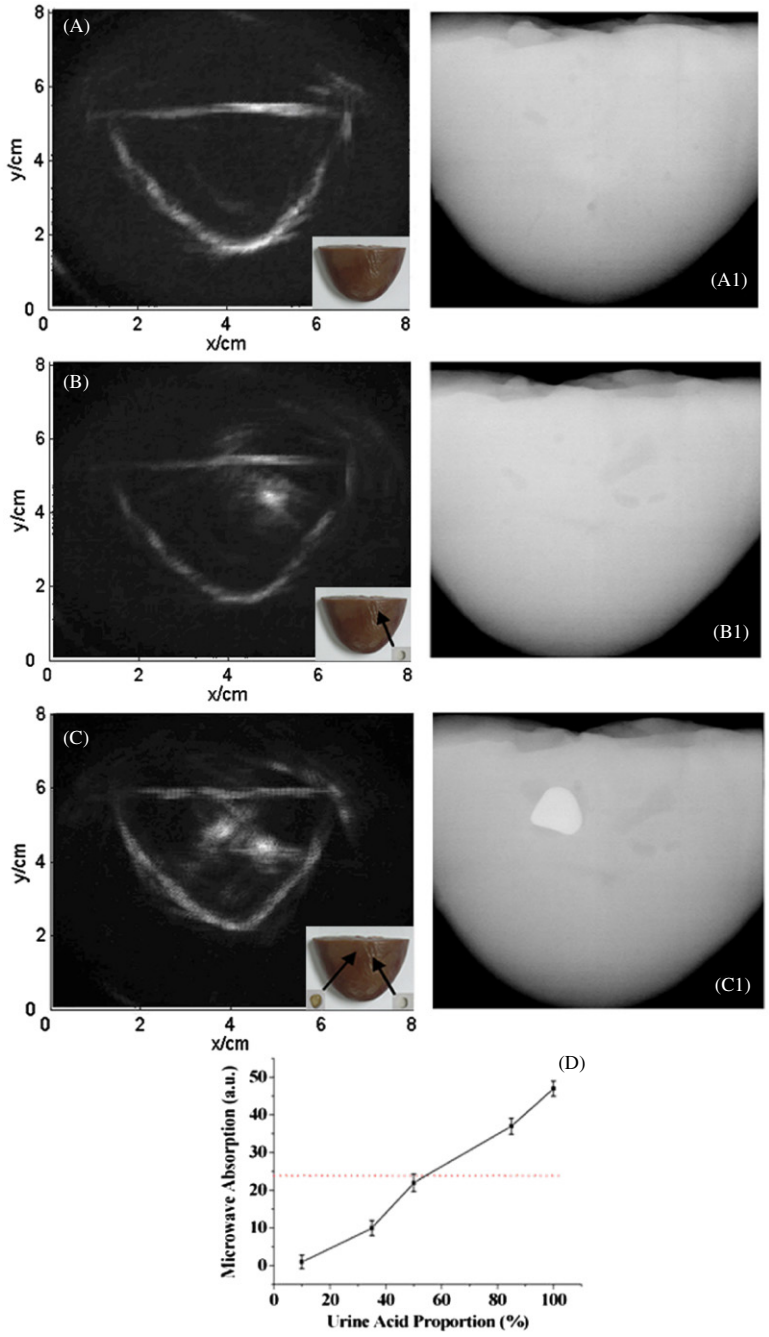

Figure 3. Thermoacoustic and x-ray imaging of the calcium oxalate calculus and uric acid calculus in the swine kidney. (A) and (A1) Reconstructed thermoacoustic image and x-ray image of the swine kidney. (B) and (B1) Reconstructed thermoacoustic image and x-ray image of the uric acid calculus placed in the swine kidney. (C) and (C1) Reconstructed thermoacoustic image and x-ray image of the calcium oxalate calculus and uric acid calculus placed in the swine kidney. (D) Graph of mixed in different proportions according to uric acid and calcium oxalate thermoacoustic absorption.

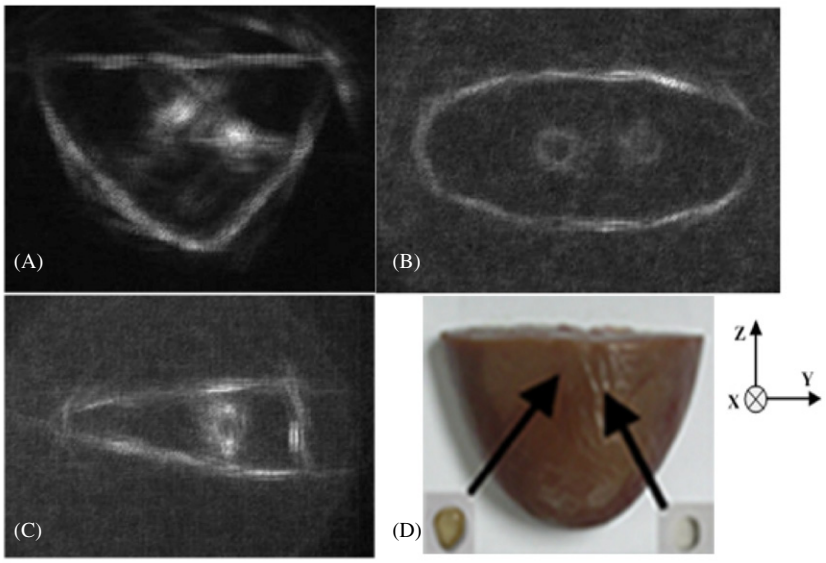

Figure 4. Orthogonal thermoacoustic images of renal calculi obtained in the kidney. (A) Coronal plane. (B) Sagittal plane. (C) Axial plane. (D) Photograph of the sample.

It is verified in our experiment that the uric acid calculus has two to three times more strong absorption coefficient of microwave than surrounding 'normal' kidney tissues at 1.2 GHz. In order to prove that the image in figure 3(B) depicts the uric acid calculus, we carried out another experiment and the results are shown in figure 3(C) and (C1). The calcium oxalate calculus and uric acid calculus are embedded at different locations of the swine kidney. The thermoacoustic image slices in figure 3(C) reveal both kinds of calculi in the processed swine kidney. It is obvious that the location and size of each calculus can be distinguished with better spatial resolution (the photograph of the samples is shown in the inset of figure 3(C)). On account of the special characteristics of the detector, only a signal due to absorption contrast can be generated but not proportional to the actual absorption; the image contrast of both kinds of calculi looks similar. Figure 3(C1) shows the x-ray image of calcium oxalate and uric acid calculus in the swine kidney. The morphology of the body outline is well illustrated. The uric acid calculus to be detected is totally unrecognizable, whereas the shape of the calcium oxalate calculus is clearly demonstrated. The reconstructed thermoacoustic images in figure 3 are in good agreement with the actual sample as shown in the inset picture. The results indicate that MI-TAT can detect the uric acid calculus and thus is superior to x-ray imaging.

It is now possible to draw a microwave absorption graph of the mixture when uric acid and calcium oxalate are in different proportions as shown in figure 3(D). The samples are mixed with uric acid and calcium oxalate powder in different proportions and solidified with a small amount of lard. The measurement is based on detecting the different proportions samples' amplitude of the thermoacoustic signals. This conclusion is deduced from the averaging of multiple sets of experimental data. It can be seen that with the concentration increase of uric acid, its microwave absorption coefficient becomes greater. When measuring pure oxalic acid, the microwave absorption is close to zero. In the graph, the red dashed line represents the microwave absorption of the normal kidney tissue. Therefore both calcium oxalate and uric acid calculus can be detected in our MI-TAT system. If the microwave absorption coefficient

of the object is much higher than that of the kidney tissue, the object can be inferred as the uric acid calculus; conversely, it is the calcium oxalate calculus.

The orthogonal images of the renal calculi model are illustrated in figure 4. The coronal (*X*–*Y* horizontal) plane of the thermoacoustic image is shown in figure 4(A), and the photograph of the sample is shown in figure 4(D). Figures 4(B) and (C) depict the locations of the sagittal (*Y*–*Z* orthogonal) and axial (*X*–*Z* orthogonal) views with the thermoacoustic imaging. In all the different orthogonal planes, the locations of the renal calculi are clearly detected. In the sagittal image, the computed distinguishing plane of the transducer array is between the two objects; hence both of them can be imaged with moderate amplitude. Since the uric acid calculus is in the computed plane while the calcium oxalate calculus is out of that plane, only one object can be found in the axial plane.

5. Conclusions

In this paper, we presented the MI-TAT method for detecting and imaging renal calculi for the first time. The calcium oxalate and uric acid calculus, embedded in swine kidney *in vitro*, were imaged by MI-TAT and x-ray. The results demonstrated that the MI-TAT method has the potential to detect the renal calculi, especially for detecting a uric acid calculus, which may fill the blind zone on the current medical detection of the renal calculi.

Acknowledgments

This research is supported by the National Basic Research Program of China (2010CB732602), the Program for Changjiang Scholars and Innovative Research Team in University (IRT0829), the National Natural Science Foundation of China (30627003; 30870676) and the Natural Science Foundation of Guangdong Province (7117865).

References

Coe F L, Evan A and Worcester E 2005 Renal stone disease *J. Clin. Invest.* **115** 2598–608

Ciocan R and Jiang H B 2004 Model-based microwave image reconstruction: simulations and experiments *Med. Phys.* **31** 3231–41

Feng D, Xu Y, Ku G and Wang L H 2001 Microwave-induced thermoacoustic tomography: reconstruction by synthetic aperture *Med. Phys.* **28** 2427–31

Finch D and Rakesh 2007 The spherical mean value operator with centers on a sphere *Inverse Problems* **23** S37–49

Gabriel S, Lau R W and Gabriel C 1996 The dielectric properties of biological tissues: II. Measurements in the frequency range 10 Hz and 20 GHz *Phys. Med. Biol.* **41** 2251–69

Guo B, Li J, Zmuda H and Sheplak M 2007 Multifrequency microwave-induced thermal acoustic imaging for breast cancer detection *IEEE Trans. Biomed. Eng.* **54** 2000–10

Guo H and Yang S H 2009 Photoacoustic tomography imaging system based on digital B-mode ultrasound diagnosis equipment *Rev. Sci. Instrum.* **80** 014903

Haltmeier M, Scherzer O, Burgholzer P and Paltauf G 2004 Thermoacoustic computerized tomography with large plain receivers *Inverse Probl.* **20** 1663–73

Haltmeier M, Schuster T and Scherzer O 2005 Filtered backprojection for thermoacoustic computerized tomography in spherical geometry *Math. Methods Appl. Sci.* **28** 1919–37

IEEE Standard 2005 IEEE standard for safety levels with respect to human exposure to radio frequency electromagnetic fields 3 kHz to 300 GHz *IEEE Stand. C95.1*

Jin X, Li C H and Wang L H 2008 Effects of acoustic heterogeneities on transcramial brain imaging with microwave-induced thermoacoustic tomography *Med. Phys.* **35** 3205–14

Jin X and Wang L H 2006 Thermoacoustic tomography with correction for acoustic speed variations *Phys. Med. Biol.* **51** 6437–48

Johnson C C and Guy A W 1972 Nonionizing electromagnetic wave effects in biological materials and systems *Proc. IEEE* **60** 692–718

Kruger R A, Kopecky K K, Aisen A M, Reinecke D R, Kruger G A and Kiser W L 1999 Thermoacoustic CT with radiowaves: a medical imaging paradigm *Radiology* **211** 275–8

Ku G, Fornace B D, Jin X, Xu M H, Hunt K K and Wang L H 2005 Thermoacoustic and photoacoustic tomography of thick biological tissues toward breast imaging *Technol. Cancer Res. Treat.* **4** 559–65

Ku G and Wang L H 2000 Scanning thermoacoustic tomography in biological tissue *Med. Phys.* **27** 1195–202

Ku G and Wang L H 2001 Scanning microwave-induced thermoacoustic tomography: signal, resolution, and contrast *Med. Phys.* **28** 4–10

Lao Y Q, Xing D, Yang S H and Xiang L Z 2008 Noninvasive photoacoustic imaging of the developing vasculature during early tumor growth *Phys. Med. Biol.* **53** 4203–12

Lou C G and Xing D 2010 Temperature monitoring utilising thermoacoustic signals during pulsed microwave thermotherapy: a feasibility study *Int. J. Hyperthermia* **26** 338–46

Nie L M, Xing D, Yang D W, Zeng L M and Quan Z 2007 Detection of foreign body using fast thermoacoustic tomography with a multi element linear transducer array *Appl. Phys. Lett.* **90** 174109

Nie L M, Xing D and Yang S H 2009 *In vivo* detection and imaging of low-density foreign boby with microwave-induced thermoacoustic tomography *Med. Phys.* **36** 3429–37

Nie L M, Xing D, Zhou Q, Yang D W and Yang H 2008 Microwave-induced thermoacoustic scanning CT for high-contrast and noninvasive breast cancer imaging *Med. Phys.* **35** 4026–32

Park H K, Kim D and Grigoropoulos C P 1996 Pressure generation and measurement in the rapid vaporization of water on a pulsed-laser-heated surface *J. Appl. Phys.* **80** 4072–81

Pelster R 2008 Bounds for local and average microwave absorption in heterogeneous systems *J. Colloid Interface Sci.* **318** 534–40

Rao P N 2004 Imaging for renal stones *World J. Urol.* **22** 323–7

Sigrist M W 1986 Laser generation of acoustic waves in liquids and gases *J. Appl. Phys.* **60** R83–121

Stefanov P and Uhlmann G 2009 Thermoacoustic tomography with variable sound speed *Inverse Problems* **25** 075011

Wang Y, Xing D, Zeng Y and Chen Q 2004 Photoacoustic imaging with deconvolution algorithm *Phys. Med. Biol.* **49** 3117–24

Xu M and Wang L H 2002 Time-domain reconstruction for thermoacoustic tomography in a spherical geometry *IEEE Trans. Med. Imaging* **21** 814–22

Xu M, Xu Y and Wang L H 2003 Time-domain reconstruction algorithms and numerical simulations for thermoacoustic tomography in various geometries *IEEE Trans. Biomed. Eng.* **50** 1086–99

Yang D W, Xing D, Gu H M, Tan Y and Zeng L M 2005 Fast multielement phase-controlled photoacoustic imaging based on limited-field-filtered back-projection algorithm *Appl. Phys. Lett.* **87** 194101

Yang D W, Xing D, Yang S H and Xiang L Z 2007a Fast full-view photoacoustic imaging by combined scanning with a linear transducer array *Opt. Express* **15** 15566–75

Yang S H, Xing D, Zhou Q, Xiang L Z and Lao Y Q 2007b Functional imaging of cerebrovascular activities in small animals using high-resolution photoacoustic tomography *Med. Phys.* **34** 3294–301

Yin B Z, Xing D, Wang Y, Zeng Y G, Tan Y and Chen Q 2004 Fast photoacoustic imaging system based on 320-element linear transducer array *Phys. Med. Biol.* **49** 1339–46

Yuan Z and Jiang H B 2006 Quantitative photoacoustic tomography: recovery of optical absorption coefficient maps of heterogeneous media *Appl. Phys. Lett.* **88** 231101

Zhang C and Wang Y Y 2008 A reconstruction algorithm for thermoacoustic tomography with compensation for acoustic speed heterogeneity *Phys. Med. Biol.* **53** 4971–82